Chapter 8

Al(Ga)InP-GaAs Photodiodes Tailored for Specific Wavelength Range

Yong-gang Zhang and Yi Gu

Additional information is available at the end of the chapter

http://dx.doi.org/10.5772/50404

1. Introduction

The sun light shining on our earth, with its main energy concentrated in visible extending to ultraviolet (UV), has activated this planet adequately. Therefore, the spectral response features of life-forms including human beings, as well as plentiful artificial creatures, are linked to those bands spontaneously and tightly. Photodiodes or photodetectors (PDs) with specific wavelength response in UV-visible bands have many practical and potential applications including ocean or water related sensing and communication, medical engineering and photodosimetry, missile guidance and countermeasures, and so on. In those wavelength bands, various groups of II-VI, III-V and VI materials could be utilized for PDs. Among them, Si PD should be the most successful one, whereas its wide response extends to near-infrared inherently, also, the performance of Si PD is limited by its indirect and relatively narrow bandgap, which restricts its applications in certain cases. Among various optional materials in those bands, the III-V Al(Ga)InP system, especially the ternary AlInP and GaInP, may work well in visible or even extending to UV band. $Al_{0.52}In_{0.48}P$ and $Ga_{0.51}In_{0.49}P$, which are lattice matched to GaAs substrate, have band gaps about 2.3 eV and 1.9 eV respectively, the combination of those two ternary materials, in conjunction with the quaternary AlGaInP system, also gives a big room in tailoring the response of the photodiodes to a specific wavelength region. Besides, profiting from the wider bandgap comparing to that of Si, higher working temperature, lower dark current and better radiation hardness could be expected for those robust materials. Furthermore, for this GaAs based III-V non-nitride system, the doping in both n and p type is feasible, a quite mature growth and processing technology can be relied on, so photovoltaic detectors and arrays with better performance could be presumed.

In this chapter, a simple review on the material issues of PDs in these bands will appear first, then concentrated on the gas source molecular beam epitaxy (GSMBE) growth of the

ternaries lattice matched to GaAs substrates, including GaInP and less-studied AlInP. The doping, structural and optical properties of the GSMBE grown materials will be investigated in detail, then turning into the growth of PD structures and processing of the device chips composing of those ternaries, mainly based on our experience. Finally, the performance of developed AlInP-GaInP-GaAs and AlInP-GaAs photodiodes tailored for specific wavelength range will be characterized and discussed.

2. Material Issues

2.1. UV-visible detector materials overview

In UV-visible bands normally quantum or photon type PDs, instead of thermal type PDs, are preferable. The materials for quantum type PDs sensitive to UV-visible bands could be chosen from group IV (e.g.: Si, SiC), group III-V (nitride, phosphide or arsenide), group II-VI (e.g.: CdS, CdTe) and so on, mainly depending on their bandgap (e.g. Razeghi et al. 1996). The expected sensitive wavelength region of a PD is mainly depending on its application requirements. Normally, inside the anticipant sensitive wavelength region a high response of the detector is expected. However, outside the anticipant sensitive wavelength region a full cutoff of the PD is preferable, because in this case the response is not a signal but noise or interference to the applications. For a quantum type PD operating in certain wavelength region, regardless of artificial resonate or filtering structures, the cutoff wavelength at long wavelength side is determined by the bandgap of the sensitive material inherently. The response of the detector at short wavelength side is depending on the material properties, device structures and so on. Normally, it will not cutoff sharply but drop continuously until reaching an unacceptable level. Furthermore, a better performance of the detector could be expected for a material with larger bandgap, regardless of some other effects. Normally the introduction of artificial resonate or filtering structures on the detection system, regardless of internally or externally, will increase the complexity, as well as cause losses, therefore a PD just matched to desired wavelength region inherently is strongly expected. Based on above considerations, when the cutoff wavelength of the detector at long wavelength side is fixed, as a rule of thumb a material with close to but slightly longer bandgap wavelength is expected. After that, the response of the detector could be finely tailored and optimized using different material stacks, device structures and processing parameters.

Quantum type PDs may have different types such as photoconductive or photovoltaic; from practical point of view photovoltaic types are more preferable because the detectors could be operated without bias, and therefore with lower dark current. In visible wavelength range group IV Si is definitely the most successful material to demonstrate photovoltaic detectors. However, its response is wider and extends to both near infrared (NIR) and UV sides. Therefore for certain applications in specific wavelength region a filter or resonate structure has to be applied to suppress the response in both long and short wavelength sides. Also, the indirect and relative narrow bandgap will limit its performance. The CdS detector has no infrared response inherently, whereas currently it only works as a photocon-

http://dx.doi.org/10.5772/50404

ductor and seems hard to reach high performance and high speed. Some other wide bandgap II-VI, SiC and III-V nitrides have also attracted much attention in those bands (e. g. Ando et al. 2002; Zhang et al. 1997; Zhang et al. 2009; Rigutti et al. 2010). Especially, various nitride AlGaN/GaN detector structures including positive-intrinsic-negative (PIN) (e. g. Pulfrey et al. 2001), Schottky (e. g. Lee et al. 2012), metal-semiconductor-metal (MSM) (e. g. Mosca et al. 2004) or metal-insulator-semiconductor (MIS) (e. g. Chang et al. 2006) have been adopted. However, their responses are mainly restricted in the UV side, and the tailoring of the response width is difficult. In addition to above-mentioned material systems, the III-V AlGaInP material system, especially the ternary AlInP and GaInP, may also work well in visible and may even extend to UV band (e. g. Zhang et al. 2005, 2010; Li et al. 2011).

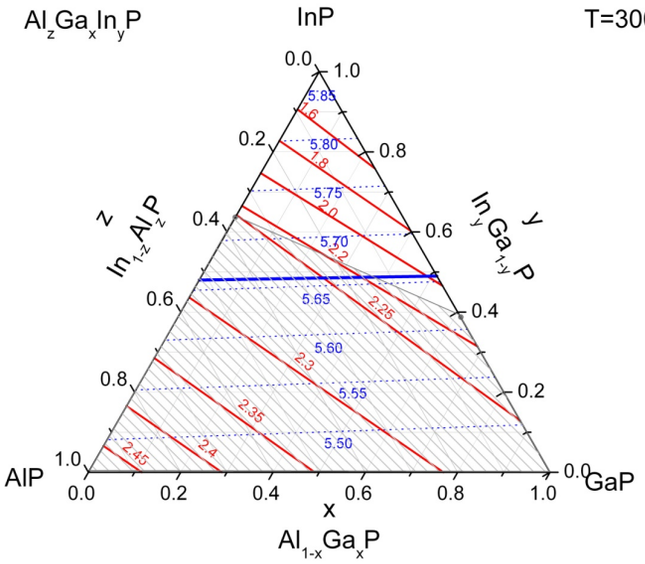

Figure 1. Lattice constant and bandgap energy of $Al_zGa_xIn_yP$ quaternary system. The shadowy bottom region indicates the indirect bandgap zone; the thick solid line in the middle indicates the quaternary alloy lattice matched to GaAs substrate.

The calculated lattice constant and bandgap energy contours of the $Al_zGa_xIn_yP$ (x+y+z=1) quaternary system are shown in Figure 1. In this figure the sloping solid line and almost aclinic dot line indicate the bandgap energies and lattice constants of this quaternary respectively. In the calculation the energy bowing of the ternary was taken into account, whereas the bowing of the quaternary was ignored. This quaternary system is composed of three group-III elements of Al, Ga and In, with only one group-V element of P. In this material system the ternaries $Al_zIn_{1-z}P$ and $Ga_xIn_{1-x}P$ are at the left and right ridges; the ternary $Al_zIn_{1-z}P$ could be recognized as the alloy of binaries indirect AlP and direct InP, and ternary $Ga_xIn_{1-x}P$ as the alloy of binaries GaP and InP also with indirect and direct bandgap, respectively. The direct bandgap of $Al_zIn_{1-z}P$ and $Ga_xIn_{1-x}P$ at 300 K could be written as E_g=3.55z +1.34(1-z)+0.48z(1-z) and E_g=2.78x+1.34(1-x)-0.65x(1-x) respectively (Vurgaftman et al. 2001). Those ternaries have the widest direct bandgap among common III-Vs excepting nitrides.

Figure 2 shows the bandgap energy and band edge wavelength of the AlInP and GaInP ternary alloys versus the indium composition x at 300 K. The materials with direct and indirect bandgap are shown by solid and dashed lines, respectively. The indium composition of the ternaries latticed matched to GaAs has also been indicated. The lattice constants of AlP and GaP are very close, which makes the indium compositions for GaAs-lattice-matched AlInP and GaInP are also very close. $Al_xIn_{1-x}P$ is lattice matched to GaAs substrate when the indium composition is around 0.48, while ternary $Ga_xIn_{1-x}P$ is lattice matched to GaAs substrate with indium composition around 0.49. It makes ternary $Al_{0.52}In_{0.48}P$ and $Ga_{0.51}In_{0.49}P$ important epitaxial materials from both research and application points of view. The $Al_{0.52}In_{0.48}P$ on GaAs shows many similar characteristics as the AlGaAs/GaAs or AlInAs/InP system. It has an indirect bandgap about 2.3 eV, which is the largest bandgap among the practical non-nitride III-V alloys, so a great deal of applications could be expected on this wide bandgap material (Gu et al. 2006, 2007). The bandgap of 2.3 eV corresponds to a cutoff wavelength of about 540 nm, which is located in the visible band. The $Ga_{0.51}In_{0.49}P$ on GaAs has a direct band gap of 1.9 eV, corresponding to the wavelength of about 650 nm. The combination of AlInP and GaInP two materials gives a room in tailoring the response of the photodiodes to a specific wavelength region in visible band and even extending to UV, but blind to infrared inherently.

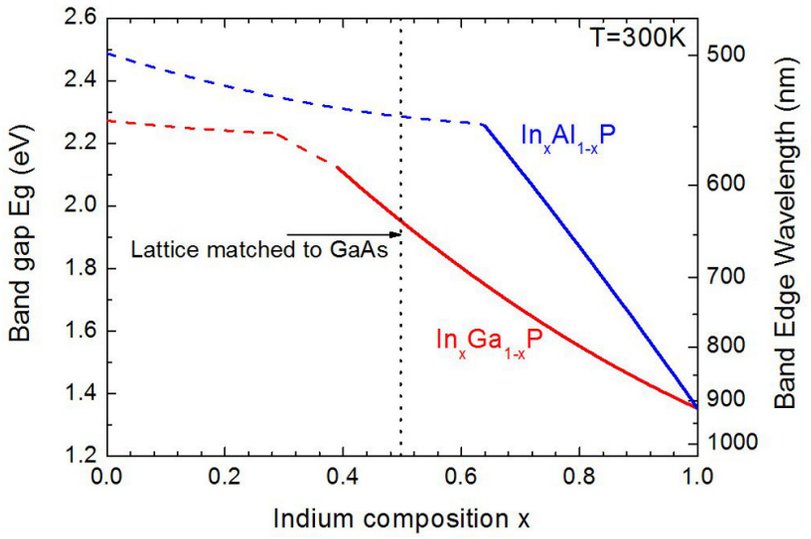

Figure 2. Bandgap energy and related band edge wavelength of $In_xGa_{1-x}P$ and $In_xAl_{1-x}P$ ternary alloys versus the indium composition x at 300 K. The materials with direct and indirect bandgap are shown by solid and dotted lines, respectively. The indium composition when the ternaries latticed matched to GaAs has also been indicated.

2.2. Gas source MBE growth of GaInP and AlInP ternary alloys

In our growth process, a VG Semicon V80H GSMBE system was applied. The best background vacuum achieved in this system was about 1×10^{-11} Torr. The elemental indium and

http://dx.doi.org/10.5772/50404

gallium Thermacells, as well as aluminum standard effusion cell, were used as group III sources, and their fluxes were controlled by changing the cell temperatures. Arsine (AsH_3) and phosphine (PH_3) high-pressure cracking cells were used as group V sources, their fluxes were pressure controlled, and the cracking temperature was around 1000 °C. Standard beryllium and silicon effusion cells were used as p- and n- doping sources, and the doping level was also controlled by changing the cell temperatures. Before the growth, the fluxes of group III sources were calibrated by using an in situ ion gauge.

The GaInP and AlInP layers were all grown on (100) oriented GaAs semi-insulating (S. I.) epi-ready substrates, which were placed on In-free Mo blocks. Prior to the growth, the surface oxide desorption of the substrate was carried out under As_2 flux. This process involved a slow ramp-up of the substrate temperature until the reflection high energy electron diffraction (RHEED) pattern shown an abrupt transformation to 2×4 surface reconstruction, in this case the substrate desorption temperature measured by thermocouple was usually about 630 °C, then the substrate temperature was decreased to appropriate temperature to begin the growth. Prior to the growth, an appropriate As-P flux exchange procedure with pump down of arsenic for 1 minute before open P flux was used. The pressure in the growth chamber during growth, which is related to the flux of group V sources, was adjusted to about 2×10^{-5} Torr. The growth rate of the epi-layers was controlled to be about 1 μm/hour, and the epi-layer thickness of all grown samples in this study was around 1 μm. After growth, the morphology of the grown samples was observed using a Normasky microscope, their structural characteristics were measured by using a Philips X-pert type X-ray diffractometer (XRD) including a Ge (220) four-folded monochrometer, and the carrier concentration of the epi-layer was determined by using Hall measurement in Van der Pauw scheme or electrochemical capacitance-voltage (EC-V) profiler at room temperature.

Ternary GaInP material has been widely applied in visible laser diodes (e.g.: Kaspari et al. 2008) and solar cells (e.g.: Geisz et al. 2008) structures. Many efforts have been paid to the epitaxy of GaInP, and found that the ordered degree plays a critical role in the growth. In our GSMBE growth, the calibration growth of GaInP layers were performed as the first step, the indium and gallium source temperatures were adjusted to grow $Ga_{0.51}In_{0.49}P$, which was lattice matched to GaAs substrate. The lattice mismatch between epilayers and substrate were confirmed by XRD measurements, the typical XRD rocking curve of grown $Ga_{0.51}In_{0.49}P$ on GaAs is shown in Figure 3. Since the thermal expansion coefficient of $Ga_{0.51}In_{0.49}P$ is larger than that of GaAs, the amount of lattice mismatch determined at room temperature is shifted to positive side comparing to the lattice match at growth temperature; therefore, at room temperature a slightly positive lattice mismatch should be preferable, the estimated lattice mismatch of $+5\times10^{-4}$ at room temperature may lead to the precise lattice match of $Ga_{0.51}In_{0.49}P$ to GaAs at growth temperature. As shown in Figure 3, the XRD measurement shows that this optimized GaInP epi-layer has a positive mismatch around $+4.9\times10^{-4}$ to GaAs substrate, with a FWHM of 28.6 arcsec for the epi-layer and 18.6 arcsec for the substrate.

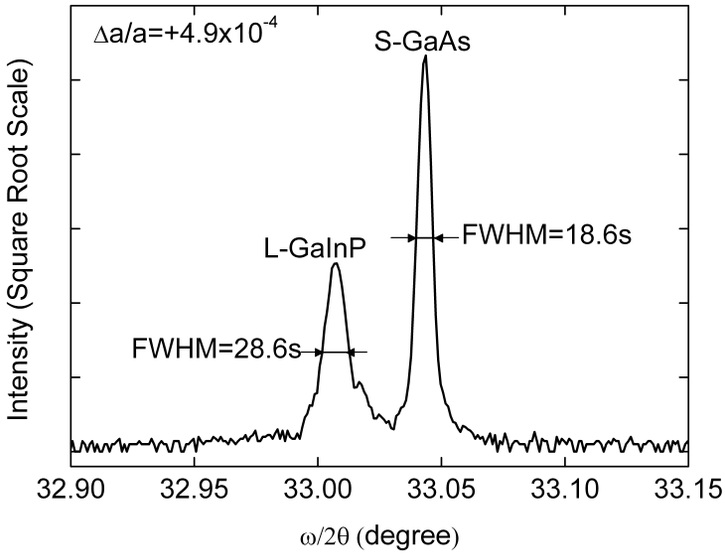

Figure 3. Measured X-ray rocking curve of typical GSMBE grown $Ga_{0.51}In_{0.49}P$ on (100) GaAs substrate.

After that, a series of $Ga_{0.51}In_{0.49}P$ layers were grown with different silicon doping levels, including an unintentionally doped sample and three samples with silicon cell temperatures of 1130 ˚C, 1150 ˚C and 1200 ˚C. The room temperature electron concentrations measured by Hall effects were high resistance, 2.4×10^{17} cm^{-3}, 1.1×10^{18} cm^{-3} and 4.6×10^{18} cm^{-3}, respectively. Photoluminescence (PL) measurements were performed for these samples and shown in Figure 4. The samples were mounted in a continuous-flow variable-temperature helium cryostat (using a HC-2D-1 APD Cryogenic System and a Lakeshore 330 temperature controller). A Coherent INNOVA 305 argon-ion laser (=514.5 nm) was used and the laser beam was focused to a spot size of approximately 0.5 mm^2 on the sample to excite the PL spectra. The PL light was collected and collimated by a couple of large quartz lens, and then focused into a Jobin Yvon THR1000 monochrometer with a 1200 grooves/mm grating, the PL signal was detected by using a photo-multiplier-tube (PMT).

It is shown in Figure 4 that the PL emission keeps nearly the same for the samples with unintentional or lower doping, the PL peaks are at 1.951 eV and the full width half-maximum (FWHM) are about 24 meV. However, as the doping level is increased to about 1×10^{18} cm^{-3}, the PL emission wavelength is blue shifted to about 1.963 eV and the peak FWHM increases to 38 meV. When the doping level is further increased to about 5×10^{18} cm^{-3}, the PL wavelength is further blue shifted to about 1.972 eV and the FWHM further increases to 58 meV. Moreover, the PL intensity for the sample with the highest silicon doping level is decreased significantly to about 1/10. The blue shift, broad FWHM and decreased intensity can be explained by the decreased ordered degree, which could be attributed to the high silicon doping (Yoon et al. 1999; Longo et al. 2001).

http://dx.doi.org/10.5772/50404

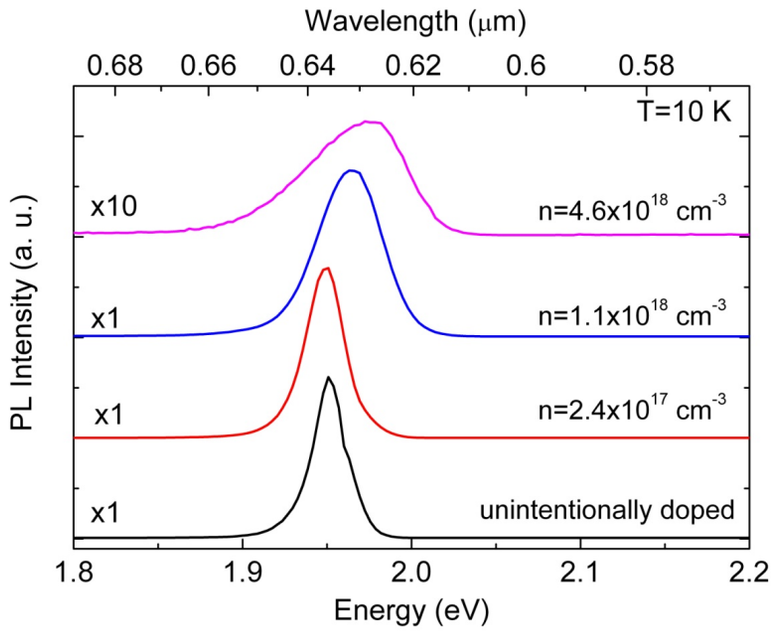

Figure 4. The PL spectra of $Ga_{0.51}In_{0.49}P$ samples with different electron concentration levels at 10 K.

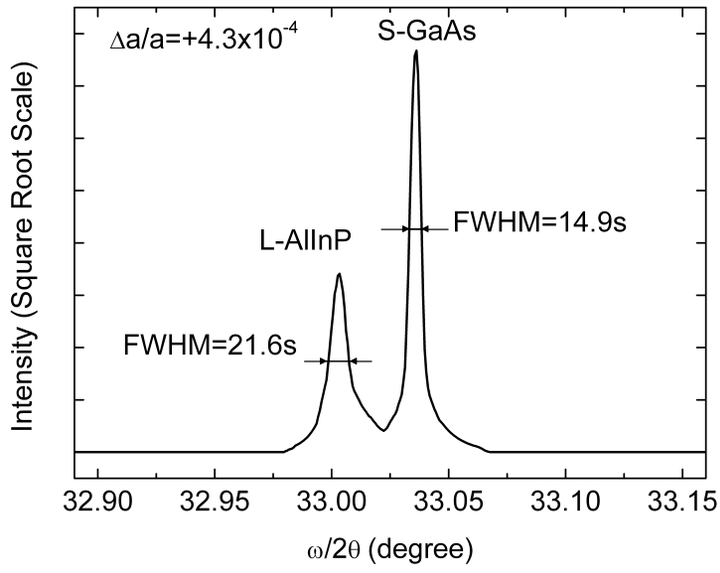

Figure 5. The AlP mole fraction versus the aluminum flux ratio η_{Al} in the GSMBE growth of AlInP.

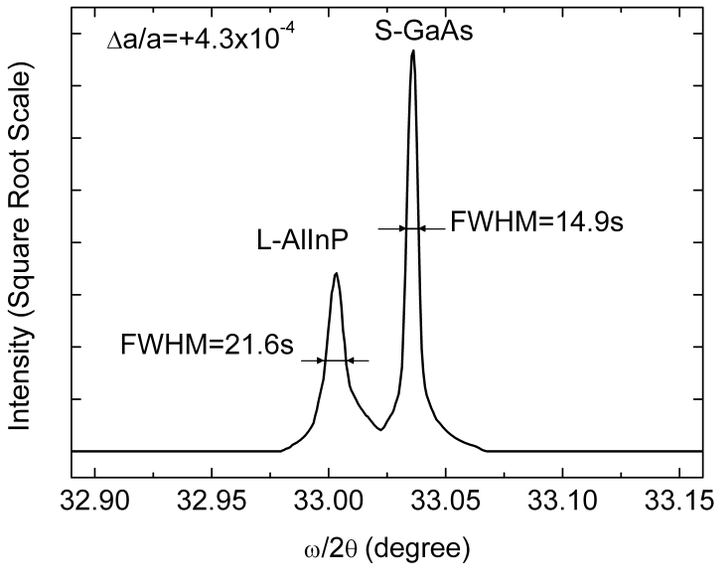

Figure 6. Measured X-ray rocking curve of typical GSMBE grown $Al_{0.52}In_{0.48}P$ on (100) GaAs substrate.

In the past years, epitaxial AlInP lattice matched to GaAs has been studied for the applications such as window/anti-reflection (AR) layer of GaInP/GaAs multi-junction solar cells (Takamoto et al. 1997; Karam et al. 2001) and cladding layer of visible lasers and modulators (Murata et al. 1991), mainly by using metal-organic chemical vapor deposition (MOCVD) techniques. The GSMBE growth of relative thin AlInP layers for the tunnel junction or window/AR layer of tandem solar cells have also been reported (Li et al. 1998). Recently, AlInP has been found with great potential to demonstrate very low dark current avalanche photodiodes (APD) (Ong et al. 2011). However, comparing with the well-developed GaInP growth, the study of the growth process and doping characteristics of AlInP on GaAs remains quite insufficient, especially for the growth of thicker and composition diversified layers. Compared to MOCVD, MBE yields a higher doping efficiency and less diffusion effects for its lower growth temperatures, and the use of gas source for group V elements in GSMBE makes the process more realizable, especially for the growth of phosphide (Gu et al. 2006& 2007).

During our GSMBE growth of ternary AlInP layers, the fluxes of aluminum and indium and their ratio in the growth of $Al_xIn_{1-x}P$ were investigated in detail. Figure 5 shows the XRD measured AlP mole fraction of AlInP versus aluminum flux ratio during the growth. The aluminum flux ratio (η_{Al}) is defined as $\eta_{Al}=f_{Al}/(f_{Al}+f_{In})$, in which f_{Al} and f_{In} is the flux of aluminum and indium cell respectively. The AlP mole fraction shows a quite linear function with η_{Al} in our experimental range, which could be used to predict the AlP mole fraction before sample growth. The non-unity slope of the line shows that indium and aluminum elements have quite different sticking coefficient, at this growth temperature the sticking coefficient of aluminum is much higher than that of indium.

http://dx.doi.org/10.5772/50404

Similar to GaInP/GaAs, a slightly positive lattice mismatch of AlInP epi-layer with respect to GaAs substrate should be preferable at room temperature. The XRD measurement shows that the optimized AlInP epi-layer has a positive mismatch around $+4.3\times10^{-4}$ to the GaAs substrate as shown in Figure 6, with a FWHM of 21.6 arcsec for the epi-layer and 14.9 arcsec for the substrate, which are among the best for epitaxial grown layers.

In this condition, a perfect mirror-like surface could be reached as shown in Figure 7(a). The Normasky micrographs of other grown samples with larger lattice mismatch to GaAs are shown in Figure 7 (b-d). Figure 7(b) shows the micrograph of AlInP epi-layer with large negative mismatch around -4.7×10^{-3}, in this condition light ripple pattern could be seen along <01$\bar{1}$> direction. At even larger negative mismatch of -6.1×10^{-3}, a cross ripple pattern along both <011> and <01$\bar{1}$> direction could be seen as shown in Figure 7(c). In negative mismatch conditions, the AlInP epi-layer is affected by tensile strain from the substrate; in this case the misfit dislocation may develop, and leads to poor morphology of the epi-wafer. However, the positive mismatched sample shows a mirror-like surface even if the mismatch reaches as large as $+7.3\times10^{-3}$ as shown in Figure 7(d). It could be deduced that the compressive strain during the growth has much weak effects on the surface morphology.

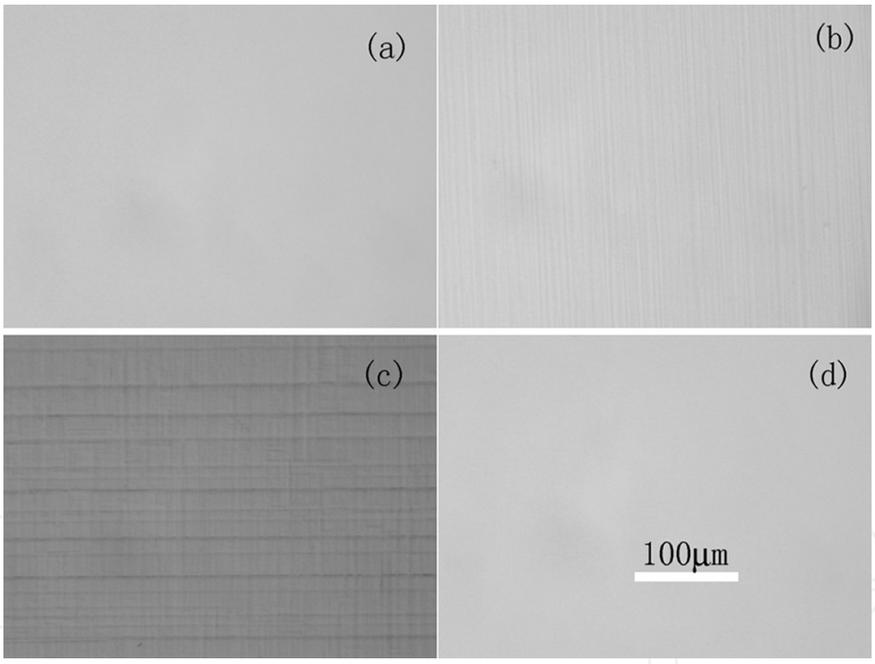

Figure 7. Normasky micrographs of the GSMBE grown AlInP epi-layers with different lattice mismatch to GaAs: (a) nearly lattice-matched layer with positive mismatch of $+4.3\times10^{-4}$; (b) layer with negative mismatch of -4.7×10^{-3}; (c) layer with even large negative mismatch of -6.1×10^{-3}; (d) layer with positive mismatch of $+7.3\times10^{-3}$.

XRD rocking curves were measured for AlInP epi-layers with different AlP mole fractions, and the FWHM of XRD epi-layer and substrate peaks as a function of AlP mole fraction is shown in Figure 8. The AlInP samples in the condition of around lattice match have narrower FWHM values and show the better lattice quality. The FWHM of epi-layer peaks kept below 100 arcsec as the lattice mismatch was in the range of about -4×10^{-3} to $+3\times10^{-3}$, and was

broadened abruptly when out of this range. The FWHM of substrate peaks was broadened to about 160 arcsec as the negative lattice mismatch was increased to -6×10^{-3}, but was still narrower than 40 arcsec as the positive lattice mismatch was increased to $+7\times10^{-3}$. It could be deduced that AlInP epi-layer with positive mismatch has better lattice quality than those with negative mismatch. This behavior also suggests that the compressive strain has weaker effects on lattice quality than the tensile strain during the growth.

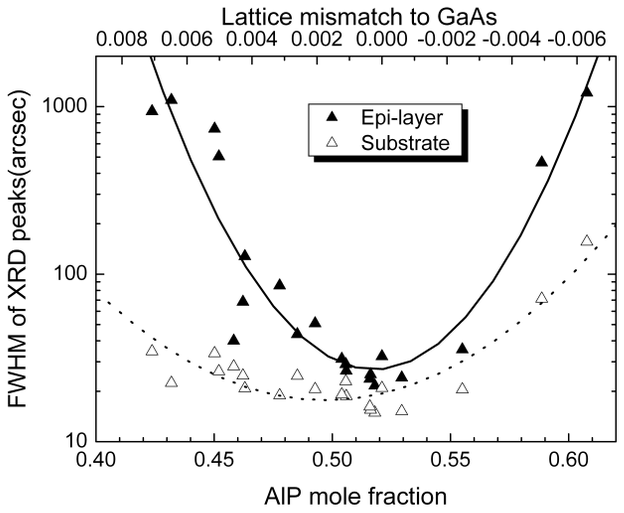

Figure 8. FWHM of XRD peaks for AlInP epi-layers and substrates versus the AlP mole fractions.

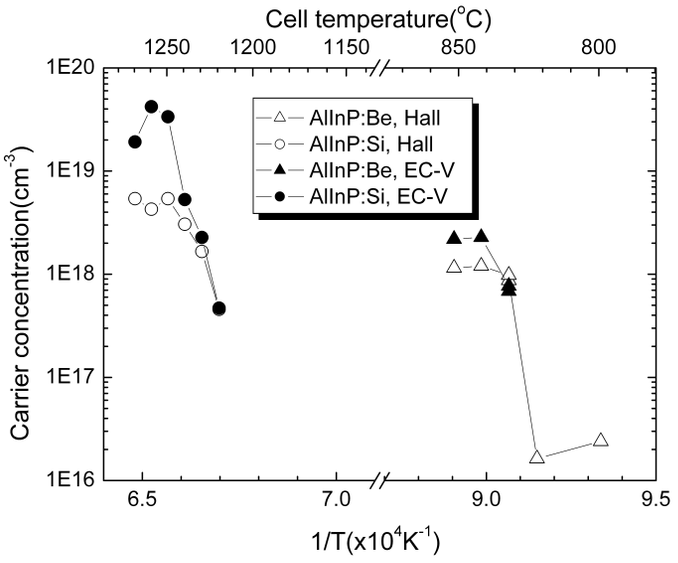

Figure 9. Average (carrier density divided by epi-layer thickness) carrier concentration in AlInP layers versus reciprocal temperature of Si and Be cells.

http://dx.doi.org/10.5772/50404

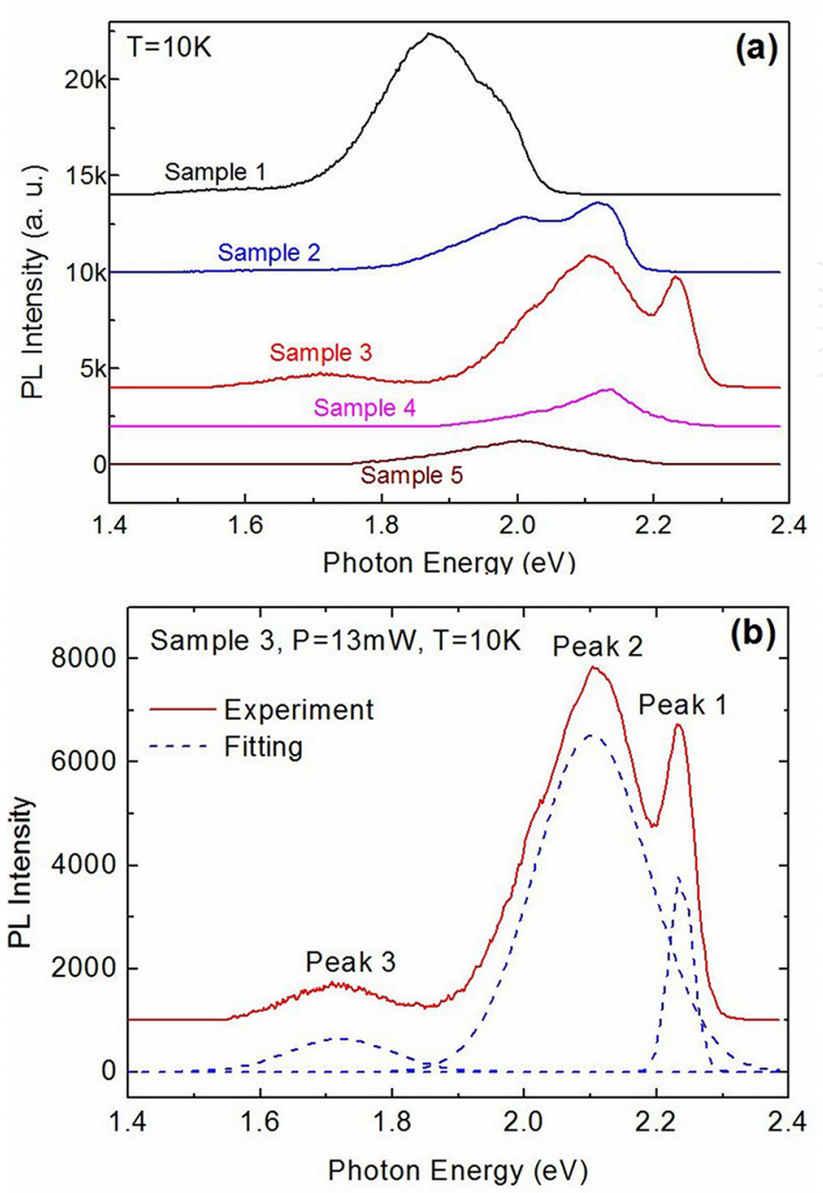

Figure 10. a) The PL spectra of five AlInP samples with different aluminum compositions at 10 K; (b) Three peaks were defined by using Gaussian fitting for PL spectrum of sample 3 at 10 K.

The electrical properties of AlInP were also investigated. Figure 9 shows the measured electron or hole concentration in Si or Be doped AlInP samples as a function of the reciprocal temperature of Si and Be cells, all those samples were around the lattice matched conditions of x=0.52. Considering that the production of two dimensional electron or hole gas is possible for higher bandgap AlInP layer grown on GaAs substrate with lower bandgap, the EC-V profiling was also done using a PN4300 Profiler, besides the Hall measurements. Regardless the measurement and system error (with a coefficient of about 2) for different measurement techniques, a good correlation between the EC-V and Hall results definitely exists. It was observed that the Hall hole concentration maintained around 10^{16} cm^{-3} as the Be cell temperature (T_{Be}) was below 820 °C, and increased to 1.2×10^{18} cm^{-3} when T_{Be} was

increased to 840 °C. Similarly, as the Si cell temperature (T_{Si}) was below 1200 °C the Hall electron concentration was quite lower, whereas as T_{Si} increased to 1250 °C the electron concentration also increased to 5.4×10^{18} cm^{-3} abruptly. At higher cell temperatures a saturation phenomenon was observed.

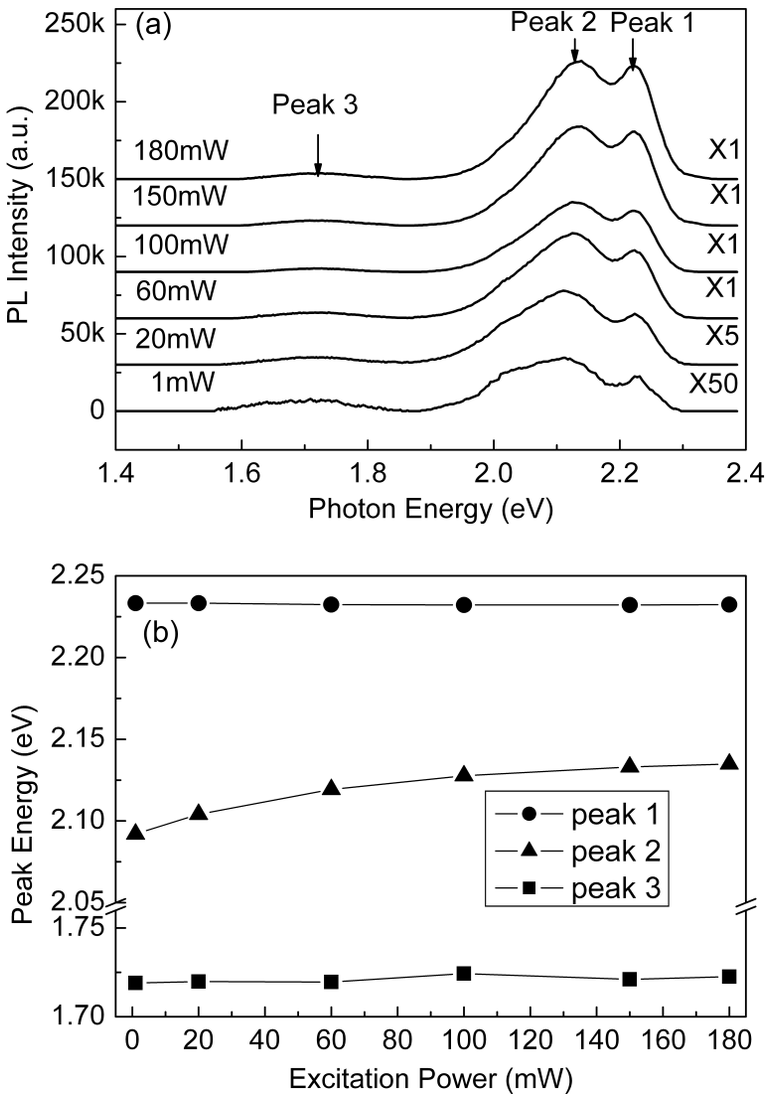

Figure 11. a) Excitation power dependence of the PL spectra for AlInP sample 3 at 10K; (b) Peak energy of the three Gaussian fitting peaks versus the excitation power for AlInP sample 3 at 10 K.

The optical properties of the grown AlInP samples were studied by using PL measurements, and the mechanisms were analyzed in detailed. Figure 10(a) shows the PL spectra of five AlInP samples with different aluminum composition at 10 K, for consistency the same exci-

http://dx.doi.org/10.5772/50404

tation power of 13 mW was used. For sample 1-5, the measured AlP mole fractions by XRD using strained estimation ($X_{Al\text{-}S}$) are 0.38, 0.40, 0.42, 0.47 and 0.51 respectively; whereas using relaxed estimation the AlP mole fractions ($X_{Al\text{-}R}$) are 0.22, 0.28, 0.32, 0.42 and 0.49 respectively. The real AlP mole fractions of these samples should be between the strained and relaxed values. Sample 1, 2 and 3 have direct bandgap, sample 5 has indirect bandgap, and sample 4 is near the critical condition. The lattice-mismatch between AlInP and GaAs substrate of sample 1 is the largest, and decreases in turn for sample 2, 3, 4, 5. As shown in Figure 10(a), several overlapped peaks, which should have different origins, could be seen in the spectra. For sample 1-3, two main peaks appear clearly, in sample 3 a weak peak also exits at lower-energy side. As the two strong peaks overlapped each other, Gaussian fitting was used to determine the peak energy and intensity exactly. In the fitting two peaks were used for sample 1 and 2, whereas three peaks for sample 3. The fitting result for sample 3 is shown in Figure 10(b), the two strong peaks are marked as peak 1 and peak 2, the weak side-peak is marked as peak 3.

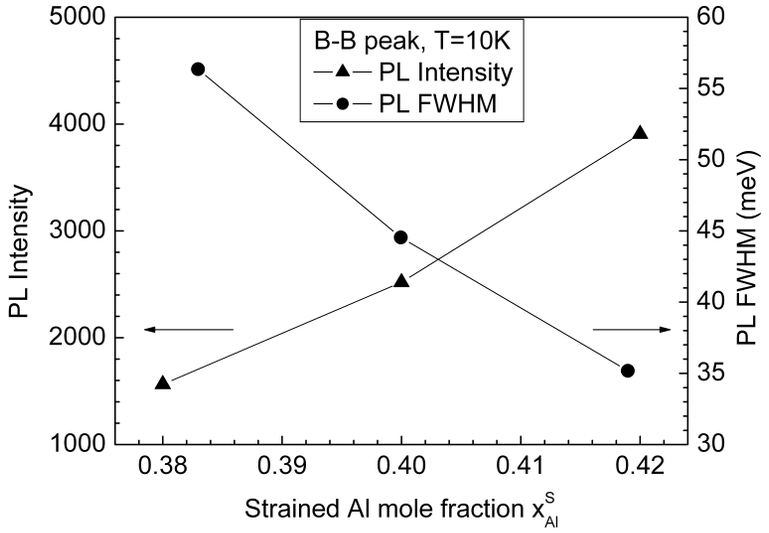

Figure 12. PL intensity and FWHM of B-B peaks for AlInP Sample 1-3 at 10K versus strained AlP mole fraction $X_{Al\text{-}S}$ at excitation power of 13 mW.

To study the origins of these emission peaks, excitation power dependence of the PL spectra was performed on sample 3 from 1 mW to 180 mW at 10 K as shown in Figure 11(a). These spectra were fitted by using three Gaussian peaks, and Figure 11(b) shows the peak energy for the three peaks as a function of the excitation power. It could be seen that peak 2 shifts to higher energy side (blue shift) as the excitation power increases, whereas no obvious shift is observed for the other two peaks. Therefore, peak 2 is considered due to shallow donor-acceptor (D-A) pair recombination, and this PL shift can be explained in terms of the Coulomb interaction of donors and acceptors as a function of their separation. As the excitation power increases, there are more probabilities for the transitions between closer D-A pairs; therefore, the emission intensity increases, and the transition energy tends to move towards high-

er energy side [Zacks et al. 1972]. On the other hand, peak 1 is deemed to be related to band-to-band (B-B) transition, which shows narrow width and not shifts as the excitation power increases. The side-peak around 1.72 eV may be considered as associated with the presence of arsenic related defects according to its peak energy and weak intensity, which may be imported by the growth background. The PL intensity and FWHM of B-B transition peak in sample 1, 2 and 3 versus the AlP mole fraction is shown in Figure 12. As AlP mole fraction increases, the intensity of B-B transition peak is increased and the FWHM is decreased, which is due to the reduction of nonradiative recombination centers and increase of the radiation efficiency in smaller lattice-mismatched material.

Table 1 lists the peak energies of the two strong peaks of B-B related E_{BB} or D-A related E_{DA} in the PL spectra, the separation energy between B-B and D-A transition peaks (E_{BB}-E_{DA}) for sample 1-3 are also listed. For sample 1-3 both the B-B and D-A transition peaks shift to higher energy side (blue shift) as AlP mole fraction increases, which is mainly caused by the increase of the bandgap. By using $X_{Al\text{-}S}$ and $X_{Al\text{-}R}$ respectively, the theoretical bandgap energies at 10 K (written as $E_{G\text{-}S}$ and $E_{G\text{-}R}$ for short) of all samples were calculated and also listed in Table 1, for sample 1-4 the Γ-valley determines the bandgap, whereas for sample 5 the X-valley has the lowest energy. For sample 1-3, the rough fraction of strained portion in the epi-layers (η) could be calculated by the linear interpolation using the following equation:

$$E_{G-S} \cdot \eta + E_{G-R}(1-\eta) = E_{BB} \tag{1}$$

The calculated results of are also listed in Table 1. Results show that this fraction increases as expected when the Al mole fraction increases and lattice mismatch decreases.

Sample No.	$X_{Al\text{-}S}$	$X_{Al\text{-}R}$	E_{BB} (eV)	E_{DA} (eV)	E_{BB}-E_{DA} (meV)	$E_{G\text{-}S}$ (eV)	$E_{G\text{-}R}$ (eV)	η (%)
1	0.38	0.22	1.98	1.87	104	2.15 (Γ)	1.83 (Γ)	47
2	0.40	0.28	2.12	2.01	117	2.19 (Γ)	1.95 (Γ)	71
3	0.42	0.32	2.23	2.10	140	2.24 (Γ)	2.02 (Γ)	95
4	0.47	0.42	NA	2.14	NA	2.34 (Γ)	2.24 (Γ)	NA
5	0.51	0.49	NA	2.00	NA	2.36 (X)	2.35 (X)	NA

Table 1. Measured and calculated data of grown AlInP samples.

It could be noticed in Figure 10(a) that the PL peaks of sample 4 and 5 have broad FWHM and weak intensity, which is because sample 4 is around the point for bandgap turning from direct to indirect and sample 5 is indirect bandgap material. The PL peaks of those two samples are considered only due to the D-A transition. As shown in Figure 10(a)and Table 1, the PL peak of sample 4 is located at 2.14 eV, whereas the peak of sample 5 is located at 2.00 eV. The strained AlP mole fraction $X_{Al\text{-}S}$ is 0.47 for sample 4 and 0.51 for sample 5, the bandgap $E_{G\text{-}S}$ at

http://dx.doi.org/10.5772/50404

10 K is around 2.34 eV and 2.36 eV for sample 4 and sample 5 respectively. It means that for sample 4 and 5 the shift direction of the PL emission peak differs from that of the bandgap energy. The analogous composition-dependent red shift of D-A transition PL peak was also reported in beryllium doped $Al_xGa_{1-x}As$ (Morita et al. 1989). In our study, the donor ionization energy (E_D) of sample 5 with X energy valley might be larger than that of sample 4 with Γ energy valley, which could induce the decrease of D-A transition energy for sample 5.

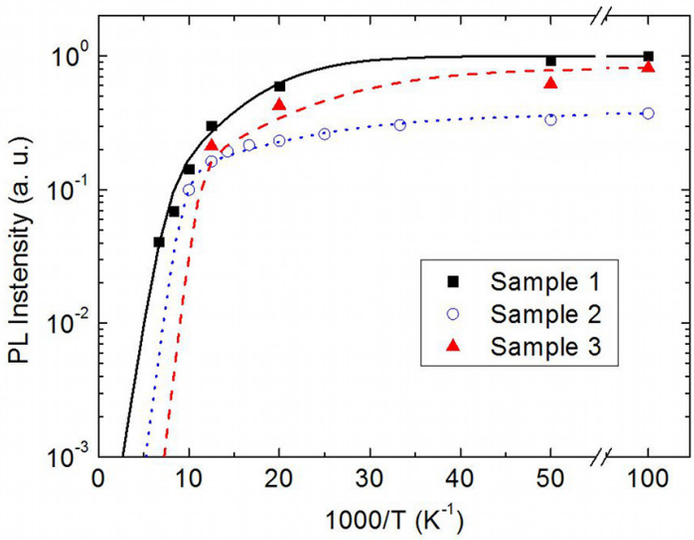

Figure 13. PL intensity of the D-A transition peak for sample 1-3 versus reciprocal temperature from 10 K to above 100 K. The solid, dotted and dashed lines are the least-squares fit of the data to Eq. (2) for sample 1-3 respectively.

The thermal activation energy and nonradiative recombination mechanism of the samples could be analyzed by the thermal quenching process of PL intensity. We have measured the PL spectra from 10 K to above 100 K at the same excitation power of 13 mW. Figure 13 shows the PL intensity of the D-A transition peak for sample 1-3 as a function of reciprocal temperature (in Log scale), and the intensities are normalized to the maximum intensity of sample 1. The curves show Arrhenius behavior with two different slopes, which could be interpreted in terms of different nonradiative recombination mechanisms respectively prevailing in two distinct temperature ranges. The slopes can give the activation energies for the two nonradiative recombination processes. The line in Figure 13 is the least-squares fit of the experimental data of D-A transition peak using the following equation as a function of temperature T [Lambkin et al. 1994 and Yoon et al. 1997]:

$$I(T) = \frac{\alpha}{1 + C_1 \exp(-E_1/kT) + C_2 \exp(-E_2/kT)} \tag{2}$$

where I(T) is PL emission intensity, α is a variable constant, and k is Boltzmann constant, C_1 and C_2 are the ratios of nonradiative to radiative recombination probabilities for the two loss

mechanisms, E_1 and E_2 are the thermal activation energies. The fitting results of E_1 and E_2 for sample 1-3 have been listed in Table 2. The obtained thermal activation energies are in the range of E_1~8-20 meV and E_2~90-120 meV without significant dependence on lattice mismatch. The thermal activation energy of E_1 is deemed to dominate at lower temperatures and be considered related to silicon donor. On the other hand, the thermal activation energy of E_2 dominates at higher temperatures. The presence of deep acceptors, such as traps or impurities, is considered to be the most likely causes of E_2. Therefore, the value of E_1 plus E_2 should indicate the total D-A pair energy. As listed in Table 2, E_1 plus E_2 is 106 meV, 116 meV and 129 meV respectively for sample 1-3, which is in good agreement with the separation energy between B-B and D-A peaks (E_{BB}-E_{DA}) as listed in Table 2.

Sample No.	E_1 (meV)	E_2 (meV)	E_1+E_2 (meV)
Sample 1	17	89	106
Sample 2	8	108	116
Sample 3	10	119	129

Table 2. Thermal activation energies estimated by fitting to the temperature-dependent PL intensity of the D-A transition peaks for sample 1-3 through Eq. (2)

2.3. Growth of Al(Ga)InP photodetector structures

Two kinds of PD epitaxy structures are grown on (100) oriented S. I. GaAs epi-ready substrates, where GaInP and AlInP are applied as absorption layers respectively (denoted as GaInP PD and AlInP PD hereafter). The GaInP PD consists of a 0.9 m n^+ GaAs buffer and bottom contact layer, a 40 nm n^+ GaInP back-surface field (BSF) layer, a 1 m n^- GaInP light absorption layer, a 60 nm p^+ GaInP emitter layer, a 30 nm p^+ AlInP window layer and a 0.2 m p^+ GaAs top contact layer, which is quite similar to the top cell structure of the tandem solar cells (e.g.: Karam et al 2001; Yamaguchi 2001). The growth of AlInP PD began with a 1 m n^+ GaInP buffer layer, which was also for the bottom contact, and then a 50 nm n^+ AlInP BSF layer was grown. After that, a 1 m n^- AlInP light absorption layer was grown, which was lightly doped with silicon to below 1×10^{16} cm^{-3} to reach fully depletion at zero bias. Finally, a 150 nm p^+ AlInP emitter layer and a 150 nm p^+ GaInP top contact layer were grown.

The grown samples all show shiny surfaces. The structural characteristics of the wafers were measured by XRD as shown in Figure 14 and Figure 15 for GaInP and AlInP PD structures, respectively. From the measurements, the epi-layer of GaInP PD shows a positive mismatch of $+9.0110^{-4}$ to the GaAs substrate, with a FWHM of 28.3 arcsec. For the AlInP PD structure, the peak of AlInP absorption layer shows a positive mismatch of $+4.7610^{-4}$ to the GaAs substrate with a FWHM of 22.5 arcsec as shown in Figure 15, confirming the good epitaxy quality. After that, the grown samples were processed into PD chips for further investigation.

http://dx.doi.org/10.5772/50404

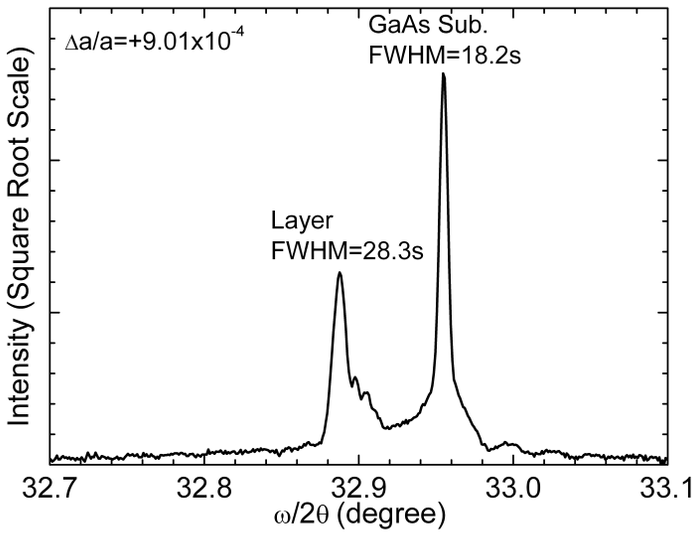

Figure 14. X-ray diffraction rocking curve of the GSMBE grown GaInP PD structure.

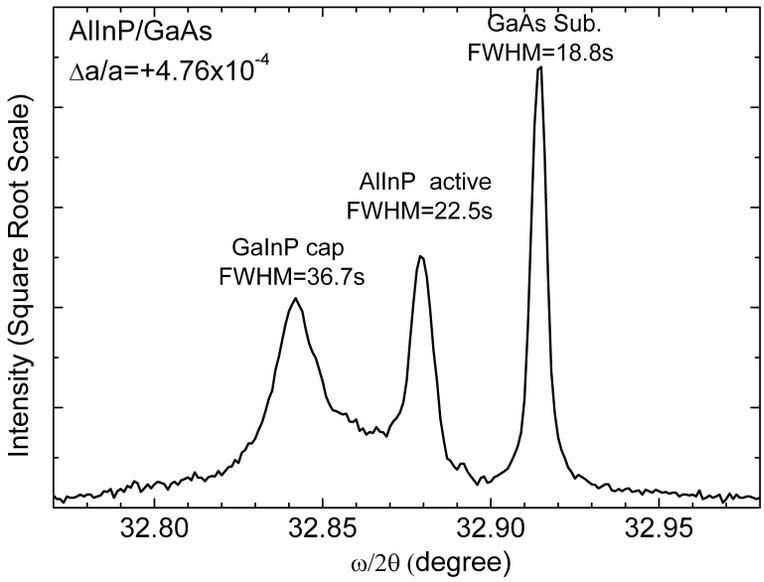

Figure 15. X-ray diffraction rocking curve of the GSMBE grown AlInP PD structure.

3. Performances of specific Al(Ga)InP photodetectors

The grown wafers were processed into mesa type PDs using conventional processing steps. The detector mesas with different diameters were defined by using photolithography and wet etching to the bottom contact layer, and then passivated by plasma enhanced chemical vapor deposition of Si_3N_4. Both the top and bottom contacts were formed using photolithography, evaporation of TiPtAu and lift-off. After an alloy step, the wafers were diced into chips, and then the chips were mounted into transistor outline (TO) packages and wire bonded for further measurements. Various photodiodes tailored for UV-enhanced or blue wavelength range was demonstrated.

3.1. UV-enhanced GaInP photodetector

As concerned in the introduction part of this chapter, many practical and potential applications need PDs sensitive to short wavelength side of visible and extending to UV, but blind to infrared. For GaInP PD, UV light may also be detected besides the visible light and blind to infrared inherently, so we can call it UV-enhanced GaInP PD as demonstrated (Zhang et al. 2005).

Figure 16 (a) shows the schematic of the GaInP detector, (b) is the capacitance-voltage (C-V) characteristics of the PD measured at 1 MHz frequency with a HP4280A C-V meter, the detector sensitive area is 1.0810^{-3} cm^2. The capacitance of this detector is 40.75 pF (37.9 nF/cm^2) at zero bias, including the capacitance of the package and bonding pad. In Figure 16, the carrier concentration along the GaInP absorption layer is also plotted, which is calculated by using $N=(1/q_0\ _rA^2)[C^3/(dC/dV)]$ and $X_d=_0\ _rA/C$ (where $X_d=0$ is at the pn junction interface) from the C-V curve. The electron concentration of $3\sim610^{16}$ cm^{-3} in the GaInP absorption layer is educed, which is in consistent with the quite low silicon doping level during the growth.

The current-voltage (I-V) characteristics, which are directly correlated to the performance of the detector, have been measured using a HP4156A precise semiconductor analyzer over more than 6 orders of magnitude in current range. Figure 17 shows the typical dark I-V characteristics of the detectors at room temperature and reverse bias. The dark current of this GaInP detector is only 340 fA at reverse bias V_R=50 mV, the breakdown voltage is great than 5 V. For those GaInP photovoltaic detectors, the output voltage under illumination is much higher than those of Si detectors, the open-circuit voltage of V_{oc}>1.05 V is measured as shown in the lower inset of Figure 17. The shunt resistances of the detector at 0 V bias (R_0) are also measured as shown in the upper inset of Figure 17, for this detector R_0 of 120 G ($R_0A=1.310^8$ cm^2) has been reached at room temperature.

http://dx.doi.org/10.5772/50404

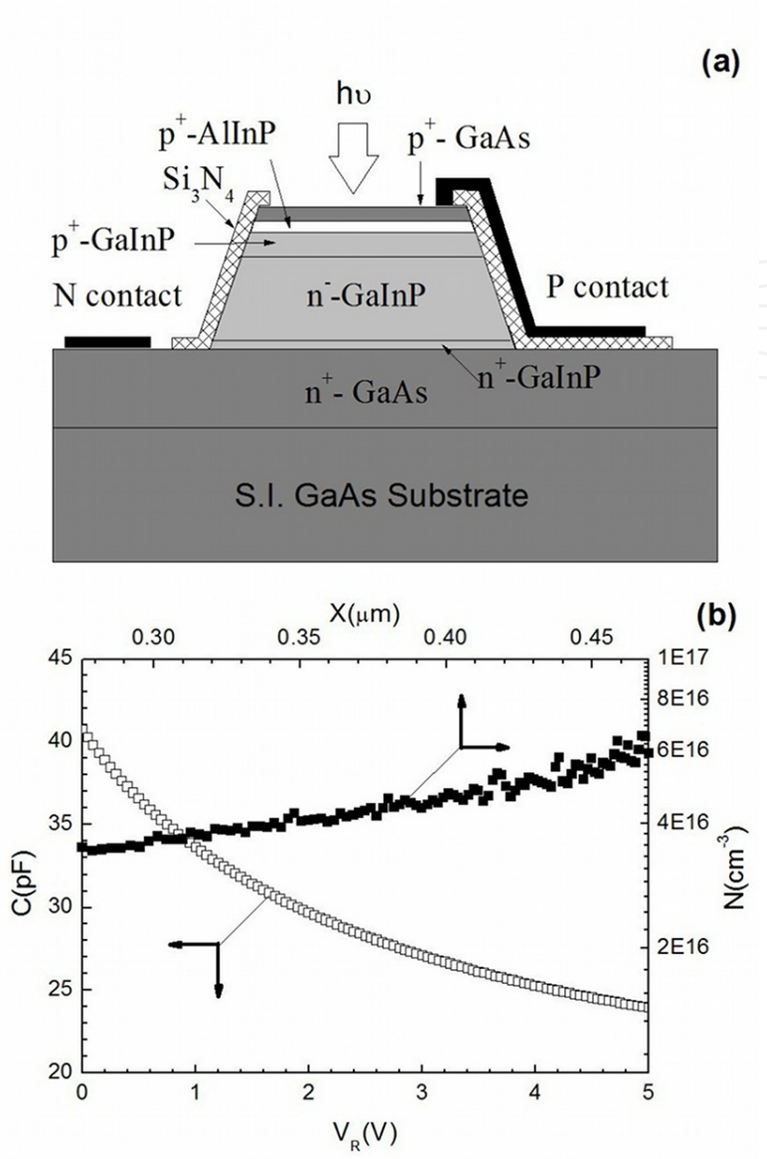

Figure 16. Schematic of the UV enhanced GaInP photodetector (a), and measured C-V characteristics of the PD and calculated carrier concentration profile in the $Ga_{0.51}In_{0.49}P$ light absorption layer.

The response spectrum of the detector was measured by using a grating monochrometer with lock-in technique, in the measurement a chopped deuterium/halogen combined light source in conjunction with a standard Si detector (with known area and calibrated responsivity data at each wavelength) was used. Figure 18 shows the measured response spectrum of the UV-enhanced GaInP PD at room temperature, the thin solid lines show the quantum efficiency grid and dashed line shows the relative C.I.E. curve of the human eye; the detector was under zero bias. It could be seen that, the response peak of the detector is at 550 nm, with 10% cut-on and cut-off wavelength of 350 nm and 675 nm, respectively. The measured responsivity of the detector at 400, 550 and 650 nm is 0.12, 0.26 and 0.19 A/W, respectively. The quantum efficiency around 500 nm reaches 60% and drops down in both red and blue

sides, besides the contact shading and non-optimized AR coating, the reduced efficiency in the red side could be contributed to the insufficient GaInP absorption layer thickness, whereas in blue side the surface recombination may play an important role. In this detector, the infrared response was totally suppressed, the measured infrared suppression ratio is greater than 250 (limited by the measurement system), whereas the UV response is enhanced evidently, this feature is desirable in certain applications. In Figure 18 the Commission International de l' Eclairage (C.I.E.) curve of human eye was also shown. Notice that the response of this detector covers the C.I.E. curve quite well, so it may also find applications in photometry.

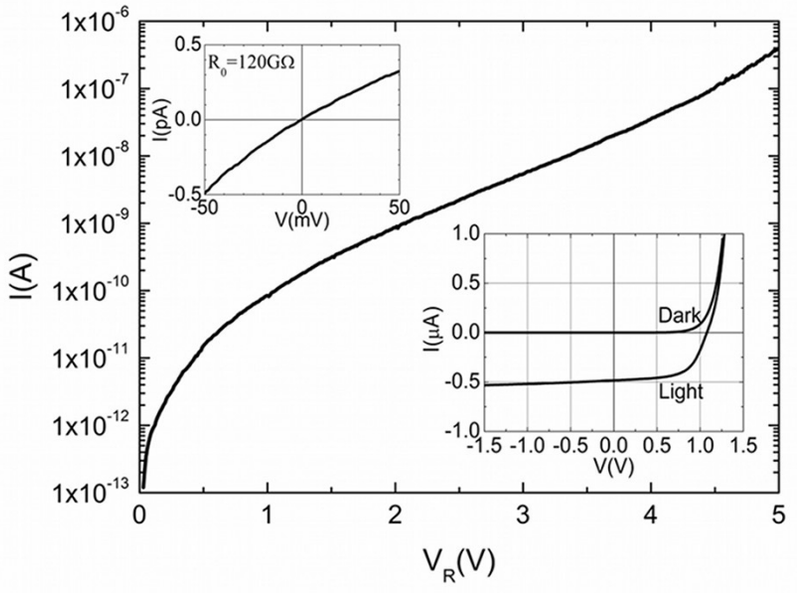

Figure 17. Measured dark I-V characteristics of the UV-enhanced GaInP PD at room temperature and reverse bias; the upper inset shows the I-V characteristics across the zero bias and related shunt resistance of the detector, the low inset shows the I-V characteristics of the detector with and without illumination.

3.2. Narrow band blue AlInP Photodetector

Clear ocean water shows attenuation minimum in the blue (450-490 nm) band with transmission peak around 480 nm, while quite sensitive to particle and pollution (Pope et al. 2000). Therefore for the ocean related remote sensing applications, sensitive PDs in this band with inherent narrow wavelength width should be needed, and photovoltaic type without filter or resonate structure is more preferable. In addition to the traditional Si, II-VI or III-V nitrides PD structures, the AlInP PD adopting AlInP as absorption layer works well in the blue band.

http://dx.doi.org/10.5772/50404

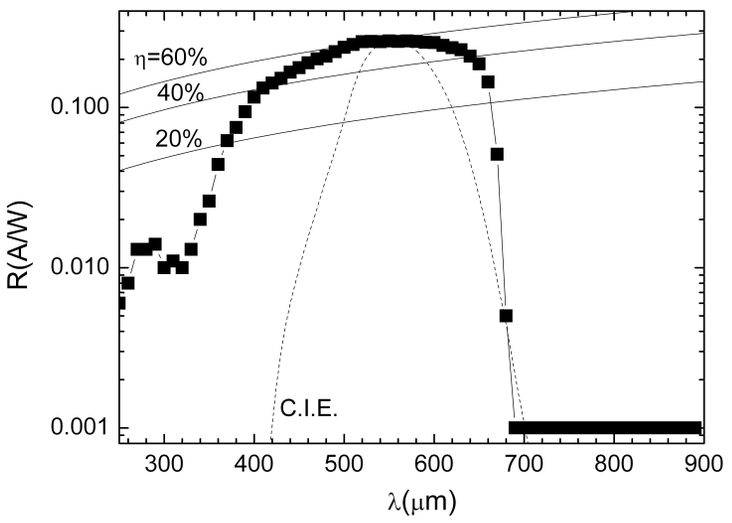

Figure 18. Measured response spectrum of the UV-enhanced GaInP PD; the thin solid lines show the quantum efficiency grid and dashed line shows the relative C.I.E. curve of the human eye.

Based on the grown AlInP PD structures mentioned above, devices have been demonstrated with the schematic structure as shown in Figure 19 (Zhang et al. 2010). The typical dark I-V characteristics of the detectors at room temperature and reverse bias are shown in Figure 20; the diameter of the detector is 300 m. It can be seen that the dark current of this AlInP/GaInP detector is only 150 fA at reverse bias V_R=500 mV, and the breakdown voltage is greater than 30 V.

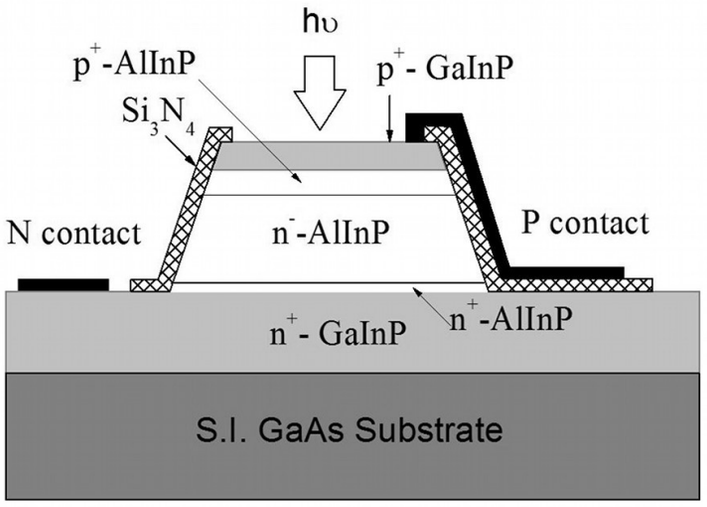

Figure 19. Schematic drawing of the AlInP blue PD.

Because of the lower doping level in AlInP absorption layer, at forward bias <1.78 V the dark current remains below 30 pA, after that the diode turns on. For those GaInP/AlInP photovoltaic detectors, the output voltage under blue light emitting diode illumination is much higher than that of Si detectors, the open-circuit voltage of V_{oc}>1.28 V is measured as shown in the lower inset of Figure 20, the illumination intensity on the detector is about 2 W. The I-V characteristics around zero bias have also been measured as shown in the upper inset of Figure 20, from which the shunt resistances of the detector at 0 V bias (R_0) are deduced. For this detector R_0 of 980 G (R_0A=6.910^8 cm^2) has been reached at room temperature.

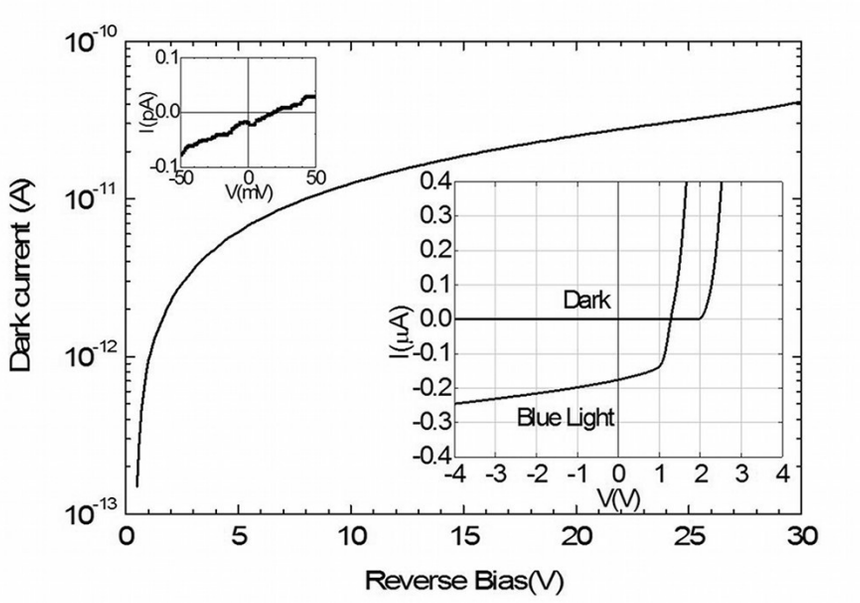

Figure 20. Measured dark I-V characteristics of the $Ga_{0.51}In_{0.49}P/Al_{0.52}In_{0.48}P$/GaAs blue photovoltaic detector at room temperature and reverse bias; the upper inset shows the I-V characteristics around zero bias, the low inset shows the I-V characteristics of the detector in dark and with blue illumination.

The response spectrum of the detector has been measured by using a grating monochrometer adopting lock-in technique. In the measurement an xenon light source chopped at 14 Hz and a calibrated $LiTaO_3$ pyroelectric detector were used. Figure 21 shows the measured responsivity spectrum of the detector under zero bias at room temperature. It could be seen that the detector has a Gaussian alike response spectrum, the peak response wavelength $_p$ is 480 nm with 50% cut-on and cut-off wavelength at 452 nm and 497 nm respectively, corresponding to a relative response wavelength width (FWHM/$_p$) of 9.4%. The measured responsivity of the detector at 480 nm and zero bias is 0.168 A/W, corresponding to an external quantum efficiency of 43.4% for this detector without AR coating. Considering ~30% reflecting loss and ~11% top contact shadowing loss, the peak internal quantum efficiency reaches 70%. In Figure 21 the absorption feature of water is also shown, the response of the detector matches the transmission window quite well.

http://dx.doi.org/10.5772/50404

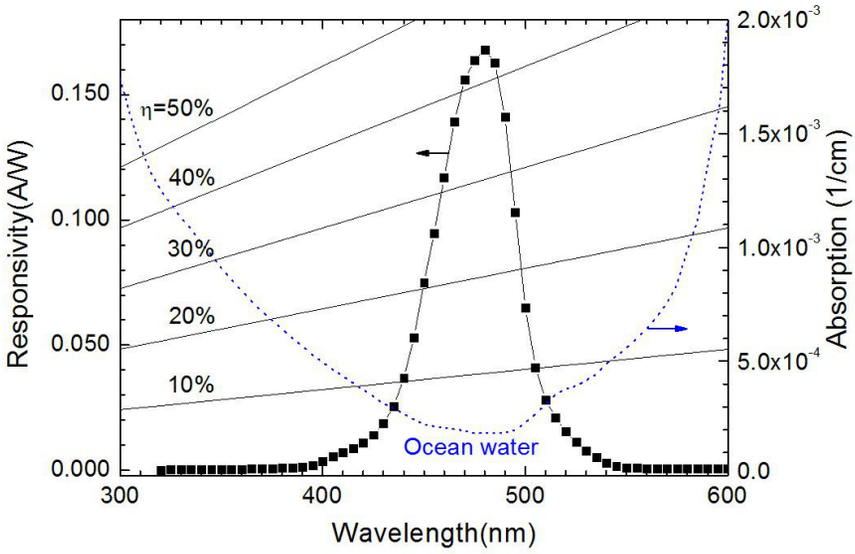

Figure 21. Measured responsivity spectrum of the AlInP blue PD; the thin solid lines show the quantum efficiency grid and dashed line shows the absorption feature of ocean water in this wavelength range.

The response of those detectors is fitly around blue band with intrinsic narrow response wavelength width, which is much lower than the normal value of above 30% for other detectors in this band. This can be attributed to our epitaxy structure design adapting the bandgap features and combination of AlInP with GaInP. At aluminum composition around 0.52 lattice matching to GaAs, AlInP is an indirect bandgap material with bandgap around 2.3 eV corresponding to wavelength about 540 nm, but enters direct bandgap around 2.6 eV (Ishitani et al. 1997; Menoni et al. 1997; Gu et al. 2006). Therefore, the absorption at blue band around 480 nm should be quite strong like those of direct bandgap material. At the same time the response at short wavelength side, especially the UV parts, is restrained by the GaInP cap layer with narrower direct bandgap of about 1.9 eV; furthermore, the response at long wavelength side is also suppressed by the use of a relative thin AlInP absorption layer. The combination of all the effects forms an appropriate response characteristic suitable for blue band detection.

For the same epitaxial structure of the detector, through the etching away of the top p^+-GaInP contact layer during the processing to open a light entrance window, the peak response wavelength of the PD blue shifted 10 nm to 470 nm as shown in Figure 22, the peak response increased obviously to 0.287 A/W (Li et al. 2011). The cut-off wavelength at short wavelength side also blue shifted 12 nm to 440 nm, whereas almost unchanged at long wavelength side. The narrow response feature of the PD still retained (increased slightly to about 12%), the dark current still kept at a quite low level (R_0A=1.710^8 cm^2), which makes this PD very useful for ocean related blue band applications.

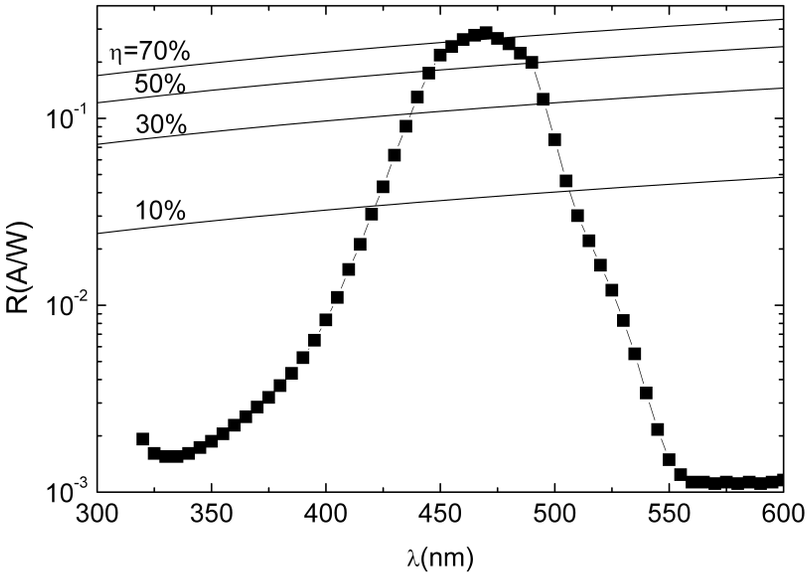

Figure 22. Measured responsivity spectrum of the AlInP PD when etching away of the top p^+-GaInP contact layer during the processing.

4. Conclusion

In conclusion, based on the analysis of the material issues for the PDs in UV-visible bands suitable for specific applications, the quaternary Al(Ga)InP system lattice matched to GaAs substrate, especially the ternaries GaInP and AlInP, were chosen as our object. Using GSMBE method, the growth techniques and material characteristics of ternaries GaInP and AlInP were investigated in detail (Gu et al. 2006, 2007). The UV-enhanced AlInP-GaInP-GaAs PD and narrow band AlInP-GaAs blue PD structures have been grown by using GSMBE, and PDs with excellent performances have been demonstrated (Zhang et al. 2005, 2010; Li et al. 2011). The spectral responses of those PDs are tailored by the design of the epitaxial and device structures to specific wavelength band, which are desirable for particular applications where selective response and outstanding performances are expected.

Acknowledgements

The authors wish to acknowledge the support of National Basic Research Program of China under grant No.2012CB619200 and Innovative Founding of Shanghai Institute of Microsystem and Information Technology, CAS.

Author details

Yong-gang Zhang* and Yi Gu

*Address all correspondence to: ygzhang@mail.sim.ac.cn

State Key Laboratory of Functional Materials for Informatics, Shanghai Institute of Microsystem and Information Technology, Chinese Academy of Sciences. Shanghai, China

References

[1] Ando, K., Ishikura, H., Fukunaga, Y., et al. (2002). Highly efficient blue-ultraviolet photodetectors based on II-VI wide-bandgap compound semiconductors. *phys. stat. sol. (b)*, 229(2), 1065-1071, 1521-3951.

[2] Chang, P. C., Chen, C. H., Chang, S. J., et al. (2006). High UV/visible rejection contrast AlGaN/GaN MIS photodetectors. *Thin Solid Films,*, 498(1-2), 133-136, 0040-6090.

[3] Geisz, J. F., Friedman, D. J., Ward, J. S., et al. (2008). 40.8% efficient inverted triple-junction solar cell with two independently metamorphic junctions. *Appl. Phys. Lett.*, 93(12), 123505, 0003-6951.

[4] Gu, Y., Zhang, Y. G., Li, H., et al. (2006). Gas source MBE growth and doping characteristics of AlInP on GaAs. *Mater. Sci. & Eng. B*, 131(1-3), 49-53, 0921-5107.

[5] Gu, Y., Zhang, Y. G., Li, A. Z., et al. (2007). Optical properties of gas source MBE grown AlInP on GaAs. *Mater. Sci. & Eng. B*, 139(2-3), 246-250, 0921-5107.

[6] Ishitani, G. Y., Nomoto, E., Tanaka, T., et al. (1997). The energy band alignment of Xc, c, and v points in $(Al_{0.7}Ga_{0.3})_{0.5}In_{0.5}P/Al_xIn_{1-x}P$ heterostructures. *J. Appl. Phys.*, 81(4), 1763-1770, 0021-8979.

[7] Karam, N. H., King, R. R., Haddad, M., et al. (2001). Recent developments in high-efficiency $Ga_{0.5}In_{0.5}P$/GaAs/Ge dual- and triple-junction solar cells: steps to next-generation PV cells. *Sol. Energy Mater. Sol. Cells*, 66(1-4), 453-466, 0927-0248.

[8] Kaspari, C., Zorn, M., Weyers, M., et al. (2008). Growth parameter optimization of the GaInP/AlGaInP active zone of 635 nm red laser diodes. *J. Crystal Growth*, 310(23), 5175-5177, 0022-0248.

[9] Lambkin, J. D., Considine, L., Walsh, S., et al. (1994). Temperature dependence of the photoluminescence intensity of ordered and disordered $In_{0.48}Ga_{0.52}P$. *Appl. Phys. Lett.*, 65(1), 73-75, 0003-6951.

[10] Lee, K. H., Chang, P. C., Chang, S. J., et al. (2012). GaN-based Schottky barrier ultraviolet photodetector with a 5 -pair AlGaN-GaN intermediate layer. *phys. stat. sol. (a)*, 209(3), 579-584, 1862-6319.

[11] Li, C., Zhang, Y. G., Gu, Y., et al. (2011). Gas source MBE grown $Al_{0.52}In_{0.48}P$ photovoltaic detector. *J. Crystal Growth*, 323(1), 501-503, 0022-0248.

[12] Li, W., Lammasniemi, J., Kazantsev, A. B., et al. (1998). GaInP/AlInP tunnel junction for GaInP/GaAs tandem solar cells. *Electron. Lett.*, 34(4), 406-407, 0013-5194.

[13] Longo, M., Parisini, A., Tarricone, L., et al. (2001). Photoluminescence investigation of superlattice ordering in organometallic vapour phase epitaxy grown InGaP layers. *Mater. Sci. & Eng. B*, 86(2-3), 157-164, 0921-5107.

[14] Menoni, C. S., Buccafusca, O., Marconi, M. C., et al. (1997). Effect of indirect -L and -X transfer on the carrier dynamics of InGaP/InAlP multiple quantum wells. *Appl. Phys. Lett.*, 70(1), 102-104, 0003-6951.

[15] Morita, M., Kobayashi, K., Suzuki, T., et al. (1989). Photoluminescence from Highly Be-Doped AlGaAs Grown by MBE. *Jan. J. Appl. Phys.*, 28(3), 553-554, 0021-4922.

[16] Mosca, M., Reverchon, J. L., Grandjean, N., et al. (2004). Multilayer (Al, Ga)N structures for solar-blind detection. *IEEE J. of Selected Topics in Quantum Electronics*, 10(4), 752-758, 0107-7260X.

[17] Murata, H., Terui, Y., Saitoh, M., et al. (1991). Low threshold current density of 620 nm band MQW-SCH AlGaInP semiconductor lasers with Mg doped AlInP cladding layer. *Electron. Lett.*, 27(17), 1569-1571, 0013-5194.

[18] Ong, J. S. L., Ng, J. S. ., Krysa, A. B., et al. (2011). Impact Ionization Coefficients in $Al_{0.52}In_{0.48}P$. *IEEE Electron Device Lett.*, 32(11), 1528-1530, 0741-3106.

[19] Pulfrey, D. L., Kuek, J. J., Leslie, M. P., et al. (2001). High UV/solar rejection ratios in GaN/AlGaN/GaN PIN photodiodes. *IEEE Trans. on Electron Devices*, 48(3), 486-488, 0018-9383.

[20] Pope, R. M., Weidemann, A. D., & Fry, E. S. (2000). Integrating cavity absorption meter measurements of dissolved substances and suspended particles in ocean water. *Dynamics of Atmospheres and Oceans*, 31(1-4), 307-320, 0377-0265.

[21] Razeghi, M., & Roraiski, A. (1996). Semiconductor ultraviolet detectors. *J. Appl. Phys.*, 79(10), 7433-7473, 0021-8979.

[22] Rigutti, L., Tchernycheva, M., Bugallo, A. D. L., et al. (2010). Ultraviolet Photodetector Based on GaN/AlN Quantum Disks in a Single Nanowire. *Nano. Lett.*, 10(8), 2939-2943, 1530-6984.

[23] Takamoto, T., Ikeda, E., Kurita, H., et al. (1997). Over 30% efficient InGaP/GaAs tandem solar cells. *Appl. Phys. Lett.*, 70(3), 381-383, 0003-6951.

[24] Vurgaftman, I., Meyer, J. R., & Ram-Mohan, L. R. (2001). Band parameters for III-V compound semiconductors and their alloys. *J. Appl. Phys.*, 89(11), 5815-5875, 0021-8979.

[25] Yamaguchi, M. (2001). Radiation-resistant solar cells for space use. *Sol. Energy Mater. Sol. Cells*,, 68(1), 31-35, 0927-0248.

[26] Yoon, I. T., Jeong, B. S., & Park, H. L. (1997). Zn diffusion of $In_{0.5}Ga_{0.5}P$ investigated by photoluminescence measurements. *Thin Solid Films*,, 300(1-2), 284-288, 0040-6090.

[27] Yoon, S. F., Mah, K. W., & Zheng, H. Q. (1999). Transport and photoluminescence of silicon-doped GaInP grown by a valved phosphorus cracker cell in solid source molecular beam epitaxy. *J. Appl. Phys.*,, 85(10), 7374-7379, 0021-8979.

[28] Zacks, E., & Halperin, A. (1972). Dependence of the peak energy of the pair-photoluminescence band on excitation intensity. *Phys. Rev. B*, 6(8), 3072-3075, 1098-0121.

[29] Zhang, T. C., Guo, Y., Mei, Z. X., et al. (2009). Visible-blind ultraviolet photodetector based on double heterojunction of n-ZnO/insulator-MgO/p-Si., *Appl. Phys. Lett.*, 94(11), 113508, 0003-6951.

[30] Zhang, Y. G., Li, A. Z., & Milnes, A. G. (1997). Metal-semiconductor-metal ultraviolet photodetectors using 6H-SiC. *IEEE Photon. Technol. Lett.*, 9(3), 363-364, 1041-1135.

[31] Zhang, Y. G., Gu, Y., Zhu, C., et al. (2005). AlInP-GaInP-GaAs UV-enhanced photovoltaic detectors grown by gas source MBE. *IEEE Photon. Technol. Lett.*, 17(6), 1265-1267, 1041-1135.

[32] Zhang, Y. G., Li, C., Gu, Y., et al. (2010). GaInP-AlInP-GaAs blue photovoltaic detectors with narrow response wavelength width. *IEEE Photon. Technol. Lett.*, 22(12), 944-946, 1041-1135.

IntechOpen